applied optics

Non-line-of-sight 2 × *N* indoor optical camera communications

Navid Bani Hassan,[1,*] Zabih Ghassemlooy,[1,2,5] Stanislav Zvanovec,[3,6] Pengfei Luo,[4,7] and Hoa Le-Minh[1,8]

[1]Optical Communications Research Group, Northumbria University, Newcastle-upon-Tyne NE1 8ST, UK
[2]QIEM, Chinese Academy of Sciences, Fujian, China
[3]Department of Electromagnetic Field, Czech Technical University in Prague, Technicka 2, 16627 Prague, Czech Republic
[4]Research Department of HiSilicon, Huawei Technologies Co., Ltd, Beijing 100085, China
[5]e-mail: z.ghassemlooy@northumbria.ac.uk
[6]e-mail: xzvanove@fel.cvut.cz
[7]e-mail: oliver.luo@hisilicon.com
[8]e-mail: hoa.le-minh@northumbria.ac.uk
*Corresponding author: navid.hassan@northumbria.ac.uk

Received 12 September 2017; revised 27 November 2017; accepted 10 December 2017; posted 12 December 2017 (Doc. ID 306843); published 7 February 2018

We propose, for the first time to the best of our knowledge, a novel non-line-of-sight 2 × *N* indoor optical camera communication system, where *N* is the number of pixels in the camera with a unique packet structure and a detection methodology for extracting the data from the recorded video streams. A comprehensive theoretical model for the proposed system is presented. The proposed system is experimentally investigated, and the measured results show that higher International Standards Organization (ISO) levels and exposure times lead to a reduced transmit power level by 3 dB for every doubling of the exposure time and ISO at a bit error rate of 10^{-3}. It is also shown that when the overlapping area of two interfering transmitters is larger than approximately 30% of the footprints, the data cannot be recovered.

OCIS codes: (230.3670) Light-emitting diodes; (040.1490) Cameras; (120.5700) Reflection; (060.0060) Fiber optics and optical communications.

https://doi.org/10.1364/AO.57.00B144

1. INTRODUCTION

The wide spread use of light-emitting diodes (LEDs) in indoor and outdoor environments has opened up growing research activities in the emerging field of visible light communications (VLC) (see [1] and the references within). Line of sight (LOS) VLC systems employing LEDs and standard photodiodes (PDs) have been adopted in many applications offering high data rates R_b over a short transmission span (1–2 m). However, LOS-based links suffer from shadowing and limited user mobility [1]. Both mobility and shadowing can be addressed by adopting (i) multi-array transmitters (Txs) and receivers (Rxs) (i.e., increased complexity); and (ii) the diffuse system but at the cost of reduced R_b (see [1,2] and the references within).

The wide spread use of smart devices equipped with LED-based screen lighting and flashlight as well as front and rear high-quality cameras offer the opportunity to establish VLC links, where the flashlight and the camera can be used as a transceiver without the need for additional hardware. The optical camera communications (OCC) offer new possibilities for the use of VLC systems in a number of applications, including display-based transmission, device to device communications (D2DC)—as part of the Internet of things—and vehicular communications where the camera-based Rx will offer multiple functionalities, including vision, data transmission, localization, and range measurement [1–6]. In contrast to the single PD-based VLC systems, a camera based Rx in OCC, which is composed of an imaging lens and image sensor (IS), has many unique features, including a wide field of view (FoV) due to the PD array, as well as spatial and wavelength separation of light beams [7].

One of the main challenges in OCC is the low frame rate of the camera, hence low data rates of OCC. However, due to the development of the complementary metal-oxide semiconductor (CMOS) image sensor technology, the quality of the captured videos with digital cameras has improved significantly in recent years. Up-to-date smartphone cameras are capable of recording video streams up to 960 frames per second (fps) at 720p resolution [8]. Moreover, similar to other multi-input multi-output systems, the complexity of the receiver is high.

The other challenge is the detection of Tx, since it covers only part of the captured image, and a number of solutions have been proposed, such as frame subtraction in both LOS [9,10] and non-LOS (NLOS) links [11], block matching [12], and vision-based image processing [13]. Also, tracking a moving object in the video stream is an issue in OCC [11,14]. Most OCC systems reported are based on the LOS path. However, in scenarios where the Txs are not within the LOS FoV, such as two vehicles approaching a cross-road, vehicles traveling on a motorway, and D2DC, the connection will be via the NLOS paths [11]. In NLOS, the reflected beams normally have large off-axis projected optical illumination footprints, which can increase the link tolerance to the camera movements. In [5,15], a rolling shutter camera was used to receive reflected lights in an indoor environment, whereas in [16], OCC demodulation based on detection of high-frequency changes of the LED light reflected from surfaces was reported for localization purposes. Despite the higher bit rate, the link span of rolling shutter-based OCC is severely limited, and the bit rate changes with the distance and the size of the optical footprint [15]. Furthermore, the detection system of rolling shutter based-OCC is highly complex.

To the best of our knowledge, in this paper for the first time, an end-to-end NLOS $2 \times N$ OCC system is proposed, which is based on a combination of successive frame subtraction, mask matching, and differential signaling schemes for detection and transmission, respectively. A unique non-standard packet structure is suggested for the proposed system, and the detection algorithm is given. We experimentally investigate the system bit error rate (BER) performance, and show that BER is improved by increasing both the International Standards Organization (ISO) and the exposure time T_{exp} of the camera. Since the proposed algorithm utilizes averaging over an area in the image, it radically reduces the impact of noise on the performance of the system. We show that a very low transmitting power of 9 mW is needed to achieve a BER of 10^{-3} at a link span of 5 m. Moreover, we investigate the impact of interference of other transmitters on the performance of the link and show that with two transmitters, if the overlapping area of the optical footprints is more than 30% of the total footprint of a single transmitter, then the signal cannot be fully recovered.

The rest of the paper is organized as follows. In Section 2, the system model is presented. In Section 3, theoretical analysis and the proposed detection algorithm are introduced. In Section 4, the experimental setup and results are discussed. Finally, Section 5 concludes the paper.

2. SYSTEM MODEL

The schematic block diagram of the proposed $2 \times N$ OCC system is shown in Fig. 1(a). At the Tx, a non-return-to-zero on–off keying (NRZ-OOK) input data stream d_l, where $l = 1, 2$, is applied to the packet generator, the output of which is differentially encoded with $x_{k,l} = x_{k-1,l} \oplus b_{k,l}$ prior to intensity modulation of LEDs. $\oplus$ represents the modulo-2 addition, $b_{k,l}$ is the output of the packet generator block, and $x_{k,l}$ is the output of the differential signaling block. Note that the initial state of modulo-2 addition x_0 is assumed to be 0, and R_b is set to half of the camera frame rate f_r. Two rectangular boxes

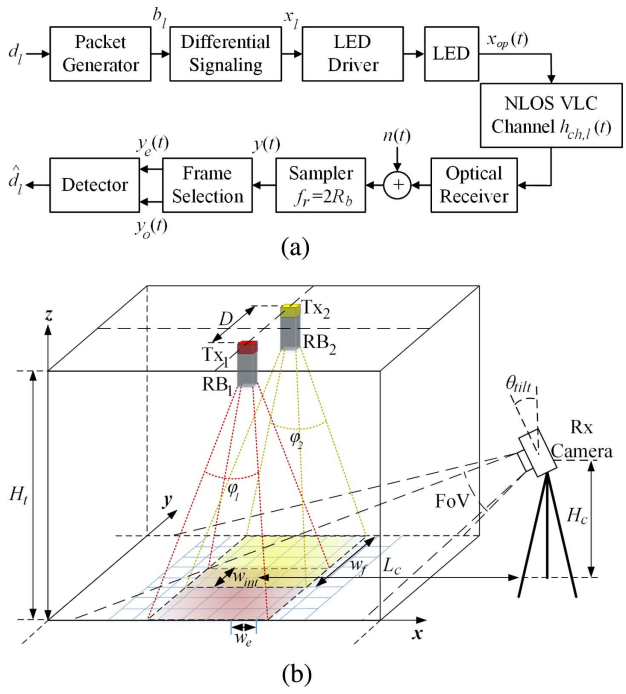

Fig. 1. Proposed OCC system: (a) schematic block diagram, and (b) system orientation with LEDs' illumination patterns. The camera is used to capture reflected lights.

(RB_1, RB_2) located in front of LEDs are used to project desired illumination patterns on to the floor [see Fig. 1(b)] creating a beam angle of $\phi_l = 2 \times \tan^{-1}(\frac{w_{RB,l}}{2H_{RB,l}})$ for each Tx, where $w_{RB,l}$ and $H_{RB,l}$ represent the width and height of boxes, respectively, and $l = 1, 2$. Figure 2 illustrates a proposed packet structure, which is composed of *start* (11-bit), *mask* (M-bit), where M is the number of Txs, and *data* (1000-bit), as in [17]. Note that a common start for both Txs can be used since LEDs are synchronized. The mask is used to determine the position of the reflected light beams from the floor, and its length depends on the number of Txs. Here, we have used two sequences of 0, 1 and 0, 0 for Tx_1 and Tx_2, respectively, which also represent the Tx's identity.

At the Rx, a typical digital camera is used to capture the reflected lights from the floor. Each video file is composed of 10 packets of 1013-bit length, which corresponds to a 5.8 min video stream. The output video stream of the camera is processed in MATLAB in order to recover d_l. In most cameras, three parameters determine the brightness of pixels: (i) shutter speed or T_{exp}—which must be smaller than $1/R_b$ in order to reduce inter-symbol interference (ISI); (ii) ISO—which determines the sensitivity of the IS; higher ISO leads to (a) increased brightness of the captured image, thereby increasing the level of perceptible shot noise (note that noise depends primarily on the overall sensor area) [18]; and (b) a decreased dynamic range

Fig. 2. Proposed packet format.

of the camera sensor; and (iii) aperture—which controls the amount of light being captured and limits or widens the depth of field. Consequently, objects located outside this range will appear hazy in the image. In non-rolling shutter-based OCC, the transmission rate is usually limited to f_r (in our proposed system, it is limited to half of f_r). For current commercial mobile phone cameras and commercial high-speed cameras, f_r are ~960 fps and >2 Mfps, respectively.

3. THEORY AND SIGNAL DETECTION ALGORITHM

At the camera, assuming a linear shift-invariant model, the received optical signal $y(t)$ is given by

$$y(t) = \mathcal{R}x_{\text{op}}(t) \otimes h(t) + n(t) + I(t), \tag{1}$$

where $x_{op}(t)$ is the transmitted optical signal, $h(t)$ is the combined impulse responses of the channel (NLOS) and the CMOS active pixel, $\mathcal{R}$ is the responsivity of each PD of the camera sensor, $I(t)$ is the interference from other light sources, and $n(t)$ is the total additive white Gaussian noise [19]. Based on [20], for NLOS, the transfer function of the link for the (i,j)th pixel of the camera is given by

$$h_{ch,l}(i,j) = \int_{p_{i-1}}^{p_i}\int_{q_{j-1}(y)}^{q_j(y)} R_{t,l}(x,y)\frac{1}{d_{t,l}^2(x,y)d_c^2(x,y)} \times A_{\text{pixel}}R_r(x,y)\rho\cos(\psi_c(x,y))\mathrm{d}A, \tag{2}$$

where A_{pixel} is the effective area of each pixel, $R_{t,l}(x,y)$ and $R_r(x,y)$ are the Lambertian radiation pattern of the LED and the reflection element, respectively, and ρ denotes the reflection coefficient of the surface. $dA = dxdy$ is the unit element area on the floor surface, where the intensity of incident light is assumed to be constant. p_i and q_j are the boundaries of the area covered by pixels in the y and x dimensions, respectively. $d_{t,l}(x,y) = \sqrt{(x-x_{t,l})^2 + (y-y_{t,l})^2 + H_t^2}$ is the distance between the Tx $(x_{t,l}, y_{t,l}, H_t)$ and the reflecting element $(x, y, 0)$, and $d_c(x,y) = \sqrt{(x-x_c)^2 + (y-y_c)^2 + H_c^2}$ is the distance between the camera (x_c, y_c, H_c) and the reflecting element. The incident angle of the camera is defined as

$$\psi_c(x,y) = \cos^{-1}(\vec{n}_l.\vec{n}_c), \tag{3}$$

where $\vec{n}_l = (x-x_c, y-y_c, -H_c)$ and $\vec{n}_c = (-\cos(\phi_{\text{tilt}})\cos(\theta_{\text{tilt}}), \sin(\phi_{\text{tilt}})\cos(\theta_{\text{tilt}}), -\sin(\theta_{\text{tilt}}))$ are the unitized incident beam and the camera plain normal vector, respectively, and the dot denotes the inner product. The frequency response of the CMOS active pixel is given by [21]

$$h_{\text{cp}}(\omega) = Ge^{-j\omega T_{\text{exp}}/2}.\frac{2\sin(0.5\omega T_{\text{exp}})}{\omega}, \tag{4}$$

where G is the amplification gain per pixel, and ω is the angular frequency. Note that the 2nd and 3rd terms represent the delay of $0.5T_{\text{exp}}$ between the center of the exposure and when the sample is actually read, and the frequency response of integrating $x(t)$ over T_{exp}, respectively. $y(t)$ is then sampled at a sampling rate $f_r = 2R_b$ (see Fig. 3) to generate a 14-bit matrix of dimensions of $(I_{\text{raw}} \times J_{\text{raw}})$ per primary color, where I_{raw} and J_{raw} are the numbers of pixels of the raw image in vertical and horizontal directions, respectively. This matrix is down-sampled

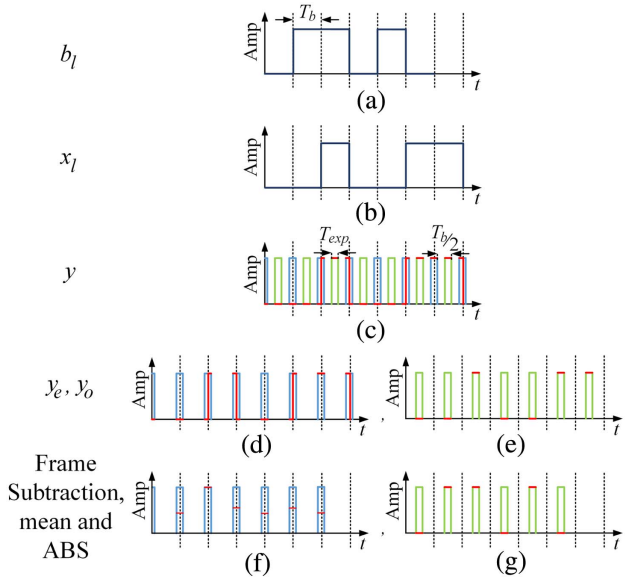

Fig. 3. Time frame of the system showing the procedures taking place on the input signal in each stage: (a) output of the packet generator, (b) differentially encoded data, (c) sampled data at $f_r = 2R_b$ using the camera, (d) even frames of the sampled data, (e) odd frames of the sampled data, (f) absolute value of the mean of subtracted even frames, and (g) absolute value of the mean of subtracted odd frames. Red lines show the value of the sampled data with the time.

to generate an 8-bit matrix of size $I \times J$ per color for the purpose of storage. Note that the sampling duration is equal to T_{exp}.

In this paper, to avoid the ISI, each bit is sampled twice to ensure that we always have a sample of the signal between the rise and fall edges. Accordingly, we define the samples in terms of two sets of odd and even samples prior to applying the detection process independently. Note that the set with a lower BER is considered. The detailed detection process at the Rx is best illustrated by a flowchart in Fig. 4. Following selection of the odd and even frames and grayscale conversion, frame subtraction is first carried out for all odd frames followed by the even frames for the entire video frame (i.e., $I \times J$ pixels) as given by

$$\Delta f_k = f_k - f_{k-1}, \tag{5}$$

where f_k and f_{k-1} are the subsequent frames. The absolute values of the mean of Δf_k for the entire array is given by

$$S_k = |\underset{i,j}{\text{mean}}(\Delta f_k(i,j))|, \qquad i = 1,\ldots,I, \qquad j = 1,\ldots,J, \tag{6}$$

where I and J are the numbers of pixels in both vertical and horizontal directions, respectively. Next, S_k is compared with a threshold level th_{St} to regenerate the start sequence, which is then correlated with the look-up-table-based bit patterns of the size 1×11. On achieving pattern matching, Flag_{St} is set to 1, and a pixelated version of the mask frames is created based on averaging over blocks of $m \times n$, where $m = n =$ 10-pixel, which is given by

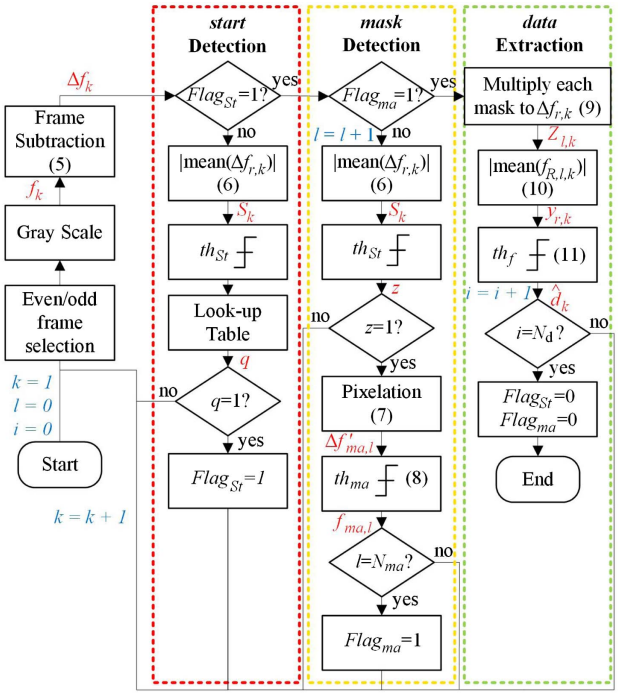

Fig. 4. Flowchart illustrating the detection process to recover the data.

$$\Delta f'_{\mathrm{ma},l}(i,j) = \underset{i,j}{\mathrm{mean}}(\Delta f_l(i,j)),$$
$$i = (\xi - 1)m + 1, \ldots, \xi m,$$
$$j = (\zeta - 1)n + 1, \ldots, \zeta n,$$
$$\xi = 1, \ldots, I/m, \quad \zeta = 1, \ldots, J/n. \tag{7}$$

Accordingly, every element of $\Delta f'_{\mathrm{ma},l}$ is binarized to form an $I \times J$ matrix. The (i,j)th pixel binary value of the lth mask frame is given by

$$f_{\mathrm{ma},l}(i,j) = \begin{cases} 1, & \Delta f'_{\mathrm{ma},l}(i,j) \geq \mathrm{th}_{\mathrm{ma}} \\ 0, & \Delta f'_{\mathrm{ma},l}(i,j) < \mathrm{th}_{\mathrm{ma}} \end{cases},$$
$$l = 1, \ldots, N_{\mathrm{ma}}, \quad i = 1, \ldots, I, \quad j = 1, \ldots, J, \tag{8}$$

where $\mathrm{th}_{\mathrm{ma}}$ is the threshold level for the mask.

Finally, for data recovery, part of the subtracted frame is multiplied by an $I \times J$ mask matrix for Tx_l, so that all non-illuminated pixels are set to zero as given by

$$Z_{l,k} = \Delta f_k . f_{\mathrm{ma},l}. \tag{9}$$

This procedure is performed for $N_{\mathrm{ma}} = 2$ times in this case, and then the mask stage flag, $\mathrm{Flag}_{\mathrm{ma}}$, is toggled to one. The mean of $Z_{l,k}$, which is a scalar number, is given by

$$y_{l,k} = \underset{i,j}{\mathrm{mean}}(Z_{l,k}(i,j)). \tag{10}$$

$y_{l,k}$ is then compared with a threshold level th_f to regenerate the transmitted data stream as given by

$$\hat{d}_{l,k} = \begin{cases} 1, & y_{l,k} \geq \mathrm{th}_f \\ 0, & y_{l,k} < \mathrm{th}_f \end{cases}. \tag{11}$$

4. EXPERIMENTAL RESULTS

Figure 5 shows the experimental setup for evaluation of the proposed system. A TTi TGA12104 arbitrary waveform generator was used to generate a pseudo random NRZ-OOK pattern of length 1000 bits. Two identical light sources, each composed of an array of 48 LEDs (chip-on-board COB LEDs) mounted on a heat sink, were placed within the tent at a height of 1.8 m and a distance of 1 m from each other. The illumination profiles of the light sources are similar to the Lambertian emission pattern of $E(\theta) = \frac{(m+1)}{2}\cos^m(\theta)$ where $m = 1$ and 2/3 in horizontal and vertical directions, respectively, and have linear optical power-current characteristics with a wide current dynamic range of 300 mA. The floor surface was covered by sheets of white paper. Figure 6(a) shows the light source's normalized illumination footprint on the floor plane, which was measured using an optical power meter. Note that the illumination level of diffracted light from the edges of rectangular boxes are about 10% of the maximum illuminance level of the light source. The floor surface area of 120 × 120 cm was divided into a number of segments of size of 3 × 3 cm, and the normalized measured reflection pattern of light reflected from each segment at a distance of 50 cm in the polar plot is depicted in Fig. 6(b), which matches with the normalized first-order Lambertian emission pattern. We observed the same profile in every segment.

A camera (Canon Rebel SL1 EOS 100D) was used to capture a 5.8 min long video stream at the RGB-colored HD resolution (i.e., 1280 × 720), and at 60 fps. The captured video was then processed off-line in the MATLAB domain, where subtracted frames were pixelated over blocks of 10 × 10 pixels in order to detect the mask. By this approach, we achieved 100 times reduction in the noise variance, thus leading to a clearer mask. All the key system parameters are shown in Table 1.

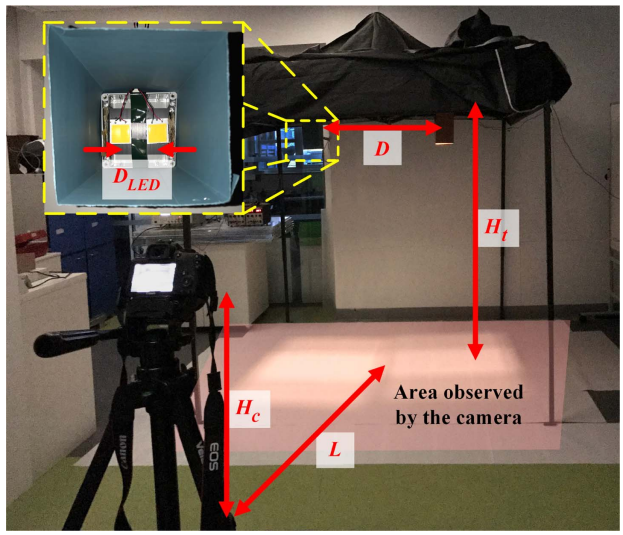

Fig. 5. Experimental setup for the proposed system and the light source shown in the inset. The floor surface is covered by sheets of white paper, and the red-highlighted area is the area that the camera observes.

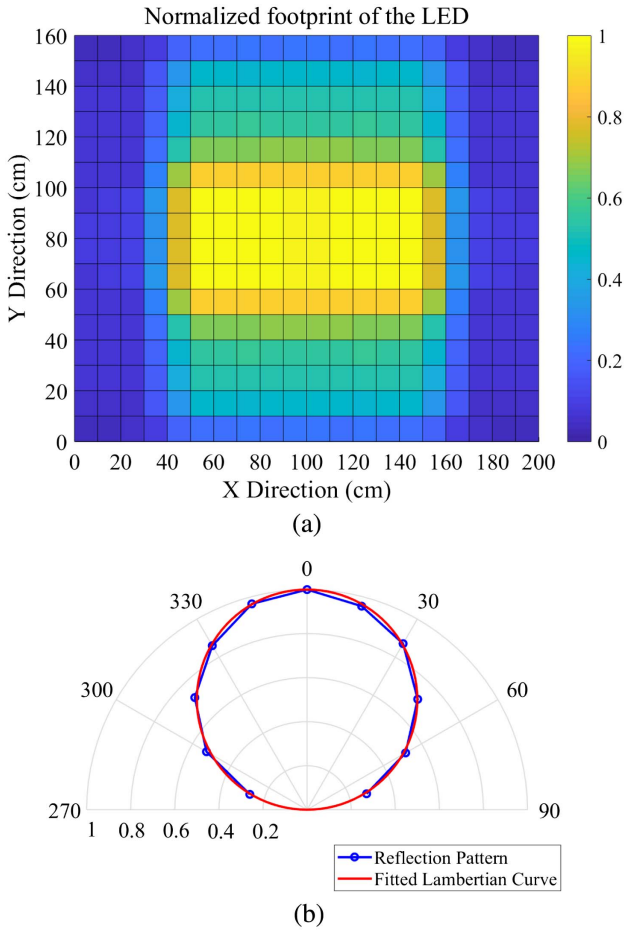

Fig. 6. Normalized: (a) footprint of the LED on the floor plane, and (b) reflection beam profile.

Figure 7 shows the measured BER as a function of the transmit power for different values of ISO, an aperture of $f4$, a shutter speed of 1/100 s, a link span of 5 m between the camera and the transmitter via a NLOS path, and a camera tilt angle of 20°. Since in this work we have adopted averaging over the area, we observe improved BER performance at higher ISOs. For example, at a BER of 10^{-3} [i.e., the forward error correction (FEC) limit], the power penalties are 3 and 6 dB for ISOs 3200 and 1600, respectively, compared to ISO 6400. This is because ISO 6400 implies doubling the pre-amplification gain compared to ISO 3200, and pixel averaging, which reduces the effect of ISO on the intensity variance. The same trend in the BER performance is also observed for a range of camera aperture of $f4$, $f5.6$, and $f8$, and $T_{\text{exp}} = 1/100$.

Next, we considered T_{exp} of the camera for a given ISO and under the focused condition. Figure 8 depicts the BER against the transmit power for a range of T_{exp} (i.e., 1/100, 1/200, 1/400, and 1/800 s) and for an aperture of $f4$. At a BER of 10^{-3}, we observe a 3 dB power penalty for every doubling of T_{exp} toward T_{exp} of 1/100. Note that increasing and decreasing T_{exp} can lead to a higher chance of capturing the rise and

Table 1. System Parameters

Symbol	Description	Value
H_t	Height of the Tx	1.8 m
D	Distance between two Txs	1 m
N_{data}	Number of payload data bits	1000 bits
N_{mask}	Number of mask bits	3 bits
N_{start}	Number of start bits	11 bits
D_{LED}	Distance between two COB-LEDs	6 cm
R_b	Transmitter bit rate	30 bps
L	Link ground span	3 m
ρ	Reflection coefficient of the floor	0.13
H_c	Height of the camera	1.3 m
f_r	Camera frame rate	60 fps
θ_{tilt}	Tilt angle	20°
f	Camera focal length	18 mm
L_{RB}	Length of the box	28 cm
A_{pixel}	Pixel area	18.4 μm^2
A_{IS}	Image sensor area	22.3 × 14.9 mm
$I_{\text{raw}} \times J_{\text{raw}}$	Camera raw image resolution	5184 × 3456
$I \times J$	Resolution of saved frames	1280 × 720

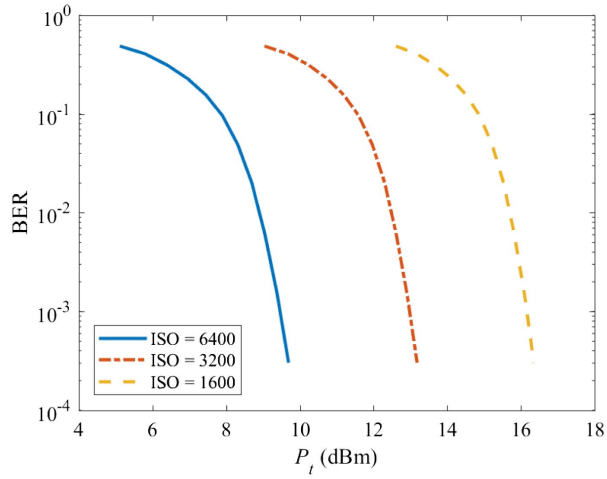

Fig. 7. BER versus the transmit power for different values of ISO, an aperture of $f4$, a link span of 5 m, and an exposure time of 1/100 s in the focused mode.

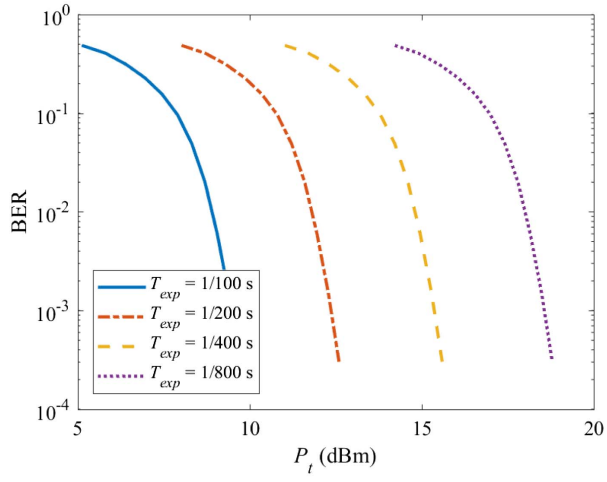

Fig. 8. BER versus the transmit power for different exposure times, an aperture of $f4$, a link span of 5 m, and ISO of 6400 in the focused mode.

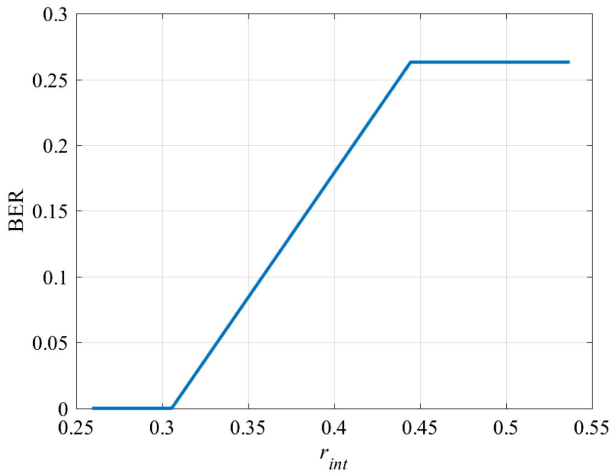

Fig. 9. BER versus width of intersection ratio, r_{int}, when two transmitters are 1 m apart for ISO of 6400, aperture of $f3.5$, exposure time of 1/100 s, and $P_t = 20$ dBm.

fall time edges of OOK-NRZ and decreasing the exposure level of the recorded image, respectively.

To find the impact of interference from other sources, we used the following parameters for the camera $T_{\text{exp}} = 1/100$ ms, aperture of f3.5, and ISO of 6400. Here, we define the intersection ratio $r_{\text{int}} = w_{\text{int}}/w_f$, where w_{int} and w_f denote the width of intersecting and the footprint area, respectively. We set the transmit power P_t to 20 dBm per the Tx. Figure 9 shows the BER performance of the proposed link as a function of r_{int}. Note that for $r_{\text{int}} > 0.3$, the BER is higher than the FEC limit, and therefore a reliable link cannot be established.

5. CONCLUSION

We have reported for the first time a novel $2 \times N$ indoor OCC system, which extracts the data information from NLOS beams. We proposed a dedicated packet structure and a detection methodology for extracting the data from the recorded video streams. An experimental test bed was developed for the proposed system. We showed that higher ISO levels and exposure times led to a reduced transmit power level by up to 6 dB for ISO of 6400 compared to ISO of 1600, and 3 dB for every doubling of the exposure time at a BER of 10^{-3}. We also showed that the proposed system works well for the intersection ratio lower than 0.3.

Funding. Engineering and Physical Sciences Research Council (EPSRC) (EP/P006280/1); Grantová Agentura České Republiky (GACR) (17-17538S).

REFERENCES

1. Z. Ghassemlooy, L. N. Alves, S. Zvanovec, and M.-A. Khalighi, *Visible Light Communications: Theory and Applications* (CRC Press, 2017).
2. A. Burton, H. Minh, Z. Ghassemlooy, E. Bentley, and C. Botella, "Experimental demonstration of 50-Mb/s visible light communications using 4 × 4 MIMO," IEEE Photon. Technol. Lett. **26**, 945–948 (2014).
3. S. Hranilovic and F. R. Kschischang, "Short-range wireless optical communication using pixilated transmitters and imaging receivers," in *IEEE International Conference on Communications* (IEEE, 2004), Vol. **2**, pp. 891–895.
4. P. Luo, M. Zhang, Z. Ghassemlooy, H. Le Minh, H.-M. Tsai, X. Tang, and D. Han, "Experimental demonstration of a 1024-QAM optical camera communication system," IEEE Photon. Technol. Lett. **28**, 139–142 (2016).
5. C. Danakis, M. Afgani, G. Povey, I. Underwood, and H. Haas, "Using a CMOS camera sensor for visible light communication," in *IEEE Globecom Workshops (GC Workkshops)* (IEEE, 2012), pp. 1244–1248.
6. P. H. Pathak, X. Feng, P. Hu, and P. Mohapatra, "Visible light communication, networking, and sensing: a survey, potential and challenges," IEEE Commun. Surv. Tutorials **17**, 2047–2077 (2015).
7. I. Takai, S. Ito, K. Yasutomi, K. Kagawa, M. Andoh, and S. Kawahito, "LED and CMOS image sensor based optical wireless communication system for automotive applications," IEEE Photon. J. **5**, 6801418 (2013).
8. Sony, "Sony Xperia XZ premium," https://www.sonymobile.com/gb/products/phones/xperia-xz-premium/specifications.
9. T. Nagura, T. Yamazato, M. Katayama, T. Yendo, T. Fujii, and H. Okada, "Tracking an LED array transmitter for visible light communications in the driving situation," in *7th International Symposium on Wireless Communication Systems (ISWCS)* (IEEE, 2010), pp. 765–769.
10. R. Boubezari, H. Le Minh, Z. Ghassemlooy, and A. Bouridane, "Novel detection technique for smartphone to smartphone visible light communications," in *10th International Symposium on Communication Systems, Networks and Digital Signal Processing (CSNDSP)* (IEEE, 2016), pp. 1–5.
11. Y. Kawai, T. Yamazato, H. Okada, T. Fujii, T. Yendo, S. Arai, and K. Kamakura, "Tracking of led headlights considering NLOS for an image sensor based V2I-VLC," in *International Conference and Exhibition on Visible Light Communications* (2015).
12. S. Arai, Y. Shiraki, T. Yamazato, H. Okada, T. Fujii, and T. Yendo, "Multiple LED arrays acquisition for image-sensor-based I2V-VLC using block matching," in *IEEE 11th Consumer Communications and Networking Conference (CCNC)* (IEEE, 2014), pp. 605–610.
13. H. Chinthaka, N. Premachandra, T. Yendo, T. Yamasato, T. Fujii, M. Tanimoto, and Y. Kimura, "Detection of LED traffic light by image processing for visible light communication system," in *IEEE Intelligent Vehicles Symposium* (IEEE, 2009), pp. 179–184.
14. S. Teli, W. A. Cahyadi, and Y. H. Chung, "Optical camera communication: motion over camera," IEEE Commun. Mag. **55**(8), 156–162 (2017).
15. W.-C. Wang, C.-W. Chow, L.-Y. Wei, Y. Liu, and C.-H. Yeh, "Long distance non-line-of-sight (NLOS) visible light signal detection based on rolling-shutter-patterning of mobile-phone camera," Opt. Express **25**, 10103–10108 (2017).
16. N. Rajagopal, P. Lazik, and A. Rowe, "Visual light landmarks for mobile devices," in *Proceedings of the 13th International Symposium on Information Processing in Sensor Networks* (IEEE, 2014), pp. 249–260.
17. T. Yamazato, I. Takai, H. Okada, T. Fujii, T. Yendo, S. Arai, M. Andoh, T. Harada, K. Yasutomi, K. Kagawa, and S. Kawahito, "Image-sensor-based visible light communication for automotive applications," IEEE Commun. Mag. **52**(7), 88–97 (2014).
18. J. Schewe, *The Digital Negative: Raw Image Processing in Lightroom, Camera Raw, and Photoshop* (Peachpit, 2015).
19. H. J. Trussell and M. J. Vrhel, *Fundamentals of Digital Imaging* (Cambridge University, 2008).
20. J. M. Kahn and J. R. Barry, "Wireless infrared communications," Proc. IEEE **85**, 265–298 (1997).
21. J. C. Chau and T. D. Little, "Analysis of CMOS active pixel sensors as linear shift-invariant receivers," in *IEEE International Conference on Communication Workshop (ICCW)* (IEEE, 2015), pp. 1398–1403.